JOURNAL OF PROPULSION AND POWER
Vol. 18, No. 5, September–October 2002

Acoustic Flutter Control of Three-Dimensional Transonic Rotor Flow

Pong-Jeu Lu,* Dartzi Pan,† and Yi-Di Yu‡
National Cheng Kung University, Tainan 70101, Taiwan, Republic of China

The fundamentals associated with the three-dimensional effects of acoustic excitation and flutter suppression in a transonic turbomachinery flow are studied. A high-resolution aeroacoustic Euler flow solver that can capture shock waves and resolve acoustic waves was developed and validated. This numerical procedure employs the modified Osher–Chakravarthy upwind total variation diminishing scheme for acoustic and discontinuity capturing. Time accuracy is accomplished by using implicit approximate lower–upper factorization together with Newton subiterations. Sound source modeling and characteristic far-field treatment are carefully implemented to result in an accurate aeroacoustic solver. Numerical simulation of a three-dimensional transonic rotor blade row (NASA rotor 67) is performed. Both internal and external acoustic excitations have been studied to investigate these acoustically excited flowfields. It is found in the present simulation that internal trailing-edge forcing is 3–5 times more effective than that excited by means of external methods, although the internal hardware implementation is much more difficult. External casing forcing of rotor 67 operated at peak-efficiency condition was also simulated. The physical mechanism of how a ducted transonic rotor flow that can be externally excited is explained. It is concluded that blade flutter in a three-dimensional turbomachine can be acoustically suppressed, either internally or externally, provided a proper control logic and sensor device is selected.

Nomenclature

A	=	Jacobian matrix
a	=	speed of sound
a_∞	=	freestream speed of sound
C_m	=	torsional moment coefficient
C_∞	=	torque coefficient
D	=	diagonal matrix
E	=	acoustic energy
e	=	total energy
$\boldsymbol{F}$	=	flux matrix
$\tilde{F}$	=	numerical flux
F_n	=	normal flux vector
f, g, h	=	Cartesian components of flux vector
G	=	gain amplitude
H	=	source term
I	=	identity matrix
$\boldsymbol{I}$	=	acoustic flux vector
k	=	reduced frequency
L	=	lower triangular matrix
M	=	Mach number
$\boldsymbol{n}$	=	unit normal vector
p	=	pressure
p'	=	pressure fluctuation
Q	=	conservative variables
Q_0	=	nondimensionlized acoustic excitation strength
R	=	flux residual
R_1	=	radius of inlet
r	=	right eigenvector
S	=	surface area
s	=	mean cell width
t	=	time variable
U	=	upper triangular matrix
$\boldsymbol{u}$	=	velocity vector
u_n	=	normal velocity component
u, v, w	=	x, y, z component of absolute velocity vector
u_r, v_r, w_r	=	x, y, z component of relative velocity vector
V	=	volume
$\boldsymbol{v}_g$	=	grid velocity vector
W	=	work
X_C	=	excitation location
x, y, z	=	Cartesian coordinates
α	=	angular deformation
γ	=	specific heat ratio
ζ, χ, δ	=	length ratios
λ	=	eigenvalue
ρ	=	density
$\tilde{\sigma}, \tilde{\tilde{\sigma}}$	=	characteristic variable differences
ϕ	=	accuracy parameter [Eq. (6)], gain phase [Eq. (17)]
Ω	=	rotational speed

Subscripts

i, j, k	=	indices designating computational cell
n	=	normal direction
Roe	=	Roe's average fluid states
∞	=	freestream condition

Superscripts

I	=	invicid
n	=	time-step index
s	=	subiteration index

Received 3 October 2001; revision received 22 April 2002; accepted for publication 20 May 2002.

*Professor, Department of Aeronautics and Astronautics. Senior Member AIAA.
†Professor, Department of Aeronautics and Astronautics.
‡Graduate Student, Department of Aeronautics and Astronautics.

I. Introduction

SUPPRESSING flutter instability using actively controlled acoustic excitation is a novel idea, first demonstrated to be feasible in a low-speed wind tunnel experiment.[1] In this innovative research both internal (a loudspeaker embedded in an airfoil) and external (a loudspeaker flush mounted in wind-tunnel wall) acoustic excitations were performed with equal success. As viewed from the hardware implementation perspective, the acoustic flutter suppression technique is quite different from those passive or active suppression methods that have been developed in the past.[2–4] The acoustic method replaces the heavy, sluggish mechanical- or

hydraulic-type actuator systems by light, electronically driven sound generators. Moreover, the frequency range that can be employed acoustically covers from a few hertz to thousands of hertz, which is not a commensurable frequency range as considered by any mechanical suppression means. These advantages attract the attention of researchers[5,6] to investigate more deeply why it works and how it can be implemented in a more pragmatic manner.

The Cambridge group led by Ffowcs Williams has been advocating this particular flutter suppression method as one of their "anti-sound" applications.[7] Acoustic or sound waves are known to be irrotational pressure disturbances that have no direct link to the circulatory aerodynamic damping needed for flutter suppression. The suppression ability of acoustic waves actually comes from the induced vortical field associated with the trailing-edge receptivity phenomenon.[8] As the emitted sound wave approaches the sharp trailing edge, vorticity waves must be shed to maintain a smooth flow, or the satisfaction of Kutta condition, at the trailing edge. According to Kelvin's theorem, these shedding vortices ought to be accompanied by a simultaneous occurrence of bound circulation variation around the airfoil, resulting in the so-called acoustically induced airloads, whose phase can be controlled to suppress the fluttering motion. This finding bridges the role of acoustics and the required aerodynamic damping for flutter suppression. Implied in this fundamental mechanism are several guidelines for the subsequent development of the acoustic flutter suppression method. First, acoustic waves are not the direct suppressing fluid power but work as a medium that triggers the acoustic/vortical conversion around the trailing edge to generate the required damping mechanism. Second, the trailing edge is the most sensitive place for an effective implementation of the acoustic suppression method. Third, the acoustic suppression method will not work when the Kutta smooth flow condition is absent, for instance, when the trailing edge is a supersonic edge or the flow is separated around the trailing edge. These guidelines are useful and have been utilized to direct the subsequent theoretical and hardware design works that are performed presently in the author's group.

For many high-performance aerodynamic designs, transonic flow is often the speed regime considered. Nevertheless, an undesirable phenomenon of low flutter boundary, termed transonic dip, often resides in the transonic regime. To overcome this low flutter boundary problem, active suppression methods are often thought of, and the acoustic method, perhaps, is the most unconventional one. Based on the success of Huang,[1] it is encouraging for the present acoustic flutter suppression research to explore more into problems associated with transonic flow. In transonic flow, a unique phenomenon that cannot be inferred or comprehended from previous experiences collected regarding subsonic excitations is the shock excursion problem. In fact, shock excursion is the major underlying mechanism responsible for low flutter boundary in the transonic flow. A feasibility study that demonstrates the suppression ability of this acoustic forcing method for flutter occurring in a transonic external flow was carried out.[9] The shock wave was shown to be moved considerably when acoustic excitations were applied. This shock excursion phenomenon was also shown to be attributed to the vortical induction effect, in addition to the direct impingement of the acoustic wave on the shock root.[9,10]

All of the mentioned works were done mainly for the two-dimensional wing flutter problems pertaining to external aerodynamics. It was proposed that acoustic flutter suppression should be more ideal for internal turbomachinery flows. This is because turbomachinery blades are shorter and stiffer and possess much higher flutter frequencies, hence are more amenable to acoustic excitation methods. Fundamental studies concerning this turbomachinery acoustic method were performed for linear cascades that are excited externally from the casing wall[11] and internally from the trailing-edge region,[12] respectively. The phenomenon of acoustically excited transonic cascade flow and the use of acoustic waves to suppress turbomachinery flutter instability were investigated numerically by Chen.[13] Initial success has been claimed for these high-frequency blade flutter control problems under the preassumption that the Kutta condition still holds at the trailing edge. Particular problems associated with these internal turbomachinery flow investigations were addressed. These problems include interblade phase angle effect, acoustic blockage effect in a ductlike passage, and the critical incidence angle effect as sound waves are sent from the downstream sources.[13]

Conceptually, using acoustic means to suppress a fluttering structure should not be viewed as a matter of energy strength. The energy or force level involved in a flutter instability, which may lead to structural disintegration, is usually much larger than those induced by acoustic means. Acoustic flutter suppression actually is a problem analogous to those of instability flow control problems.[7,14] The initiation of the control actuator for suppressing an instability, no matter whether it originates in fluids or structures, ought to be the sooner the better, when the growing disturbances are still small. As energy builds up, when disturbances are drastically amplified to a significant extent due to the system instability, there is literally no chance that any existing acoustic methods would work effectively. For the present acoustic flutter control problem, it is speculated that with a proper sensor design, in principle, there should exist some time window in which the instability amplitude, as growing from an infinitesimal perturbation, is still small so that the acoustically induced control forces can be of use to suppress the flutter instability.

In this work, the NASA rotor 67 is taken as the physical model for evaluating the present active acoustic control method. Both internal (blade trailing edge) and external (casing or hub) forcing scenarios are examined. To simplify the flow analysis and, hence, make the unsteady three-dimensional simulation tractable, the tip-leakage flow of the turbomachine is neglected for the time being. Inviscid Euler flow simulations were conducted to unveil the primary turbomachinery flow structure under acoustic excitations. The peak-efficiency flowfield of a single-staged rotor 67 is assumed as the mean flow to be excited. The tip relative Mach number in this optimal operational condition is supersonic, $M_r = 1.38$. As casing forcing is applied, how this excitation reaches the subsonic core flow and induces airloads therein is explained. This nonuniform mean shear stream constitutes an important three-dimensional effect that has to be understood when acoustic disturbances are to be applied external from the turbomachinery casing.

A hypothetical single-degree-of-freedom pitching flutter and flutter suppression by means of acoustic excitation is investigated. The importance of appropriate control logic and proper timing of control activation is addressed. A practical concern of the required acoustic strength and energy content is also raised and discussed. All of the understanding gained will be valuable for the subsequent acoustic flutter experiment to be carried out in the future.

II. Finite Volume Discretization

The unsteady, three-dimensional inviscid Euler flow in a domain V bounded by a surface S can be expressed in an integral conservation form,

$$\frac{\partial}{\partial t}\int_V Q\,\mathrm{d}V + \oint_S \boldsymbol{F}\cdot\boldsymbol{n}\,\mathrm{d}S = \int_V H\,\mathrm{d}V \tag{1}$$

in which the conservative variables Q, the normal flux vector $F_n = \boldsymbol{F}\cdot\boldsymbol{n}$, and the source term H are given, respectively, by the column vectors

$$Q = \begin{bmatrix} \rho \\ \rho u \\ \rho v \\ \rho w \\ \rho e \end{bmatrix}, \qquad F_n = \begin{bmatrix} \rho(u_n - v_n) \\ \rho u(u_n - v_n) + pn_x \\ \rho v(u_n - v_n) + pn_y \\ \rho w(u_n - v_n) + pn_z \\ \rho e(u_n - v_n) + pu_n \end{bmatrix}$$

$$H = \begin{bmatrix} 0 \\ 0 \\ \rho w\Omega \\ -\rho v\Omega \\ 0 \end{bmatrix} \tag{2}$$

where $u_n = \boldsymbol{u}\cdot\boldsymbol{n}$ is the normal velocity component, $v_n = \boldsymbol{v}_g\cdot\boldsymbol{n}$ is the normal grid velocity component, Ω is the rotational speed about the x axis, and $\boldsymbol{n}$ is the unit outward normal of the boundary S. These equations are written in a rotating Cartesian coordinate system attached to the moving blade. The variables p and e are the static pressure, and specific total energy, respectively. In closing these governing equations, the thermodynamic state equation of a perfect gas is assumed,

$$p = (\gamma - 1)[\rho e - (\rho/2)\boldsymbol{u}\cdot\boldsymbol{u}] \tag{3}$$

in which the specific heat ratio is given by $\gamma = 1.4$.

Note that (u, v, w) and (u_r, v_r, w_r) are the absolute and the relative velocity components, respectively, in the rotating coordinate system. The following relationships hold among the various velocity components:

$$u_r = u, \qquad v_r = v + \Omega z, \qquad w_r = w - \Omega y \tag{4}$$

Absolute velocity components are used in the numerical computation. However, in the analysis of flowfield physics, the relative velocity components are more convenient.

In a finite volume approach, Eq. (1) can be applied to each cell to result in a semidiscreted form

$$\frac{\partial}{\partial t}(Q_{i,j,k}) = -\sum_m \tilde{F}_m S_m + HV_{i,j,k} = -R(Q) \tag{5}$$

where S_m is the surface area and the index m refers to the mth external side of the control volume $V_{i,j,k}$. The value $Q_{i,j,k}$ is cell averaged over the control volume, and $R(Q)$ is termed the flux residual.

The numerical flux function $\tilde{F}_m$ dictates the nature and order of accuracy of the scheme. The details of the numerical method currently adopted may be found in Ref. 15 and is highlighted as follows. The spatial accuracy of the finite volume discretization depends on the construction of the numerical flux function specified at the cell interface. In this study, to capture tiny acoustic disturbances, the original Osher–Chakravarthy MUSCL-type upwind scheme[16] based on Roe splitting[17] is modified. Modification has been made on the interpolation of cell interface values and takes into account the grid nonuniformity effect. For a time-accurate acoustic computation, this refinement of interpolation is crucial to reduce spurious high-frequency numerical waves occurring within the grid system.[15]

At each i direction cell interface $i + \frac{1}{2}$, let $Q^+_{i+1/2}$ and $Q^-_{i+1/2}$ be the values of the conservative variables specified at the right and left sides of the cell interface. This modified Osher–Chakravarthy MUSCL-type upwind total variation diminishing[16] scheme takes the following form[10,15]:

$$Q^-_{i+\frac{1}{2}} = Q_i + \chi_i \sum_m \left[(\zeta_i + 2\phi\delta_i)\tilde{\sigma}^m_{i+\frac{1}{2}} + \frac{1}{\zeta_i}(1 - 2\phi\delta_i)\tilde{\sigma}^m_{i-\frac{1}{2}}\right] r^m_i$$

$$Q^+_{i-\frac{1}{2}} = Q_i + \chi_i \sum_m \left[(\zeta_i - 2\phi\delta_i)\tilde{\sigma}^m_{i+\frac{1}{2}} + \frac{1}{\zeta_i}(1 + 2\phi\delta_i)\tilde{\sigma}^m_{i-\frac{1}{2}}\right] r^m_i \tag{6}$$

in which $\sigma^m_{i\pm 1/2}$ is the characteristic variable difference, r^m_i is the mth right eigenvector of the flux Jacobian matrix, and the geometry-related parameters ζ_i, χ_i, and δ_i are functions of the mean cell width s_i (defined as the length of a straight line segment connecting the centers of the two opposite cell surfaces) in the i direction:

$$\zeta_i = \frac{s_i + s_{i-1}}{s_i + s_{i+1}}, \qquad \chi_i = \frac{s_i}{s_{i+1} + 2s_i + s_{i-1}}$$

$$\delta_i = \frac{s_i}{s_i + s_{i+1}} \tag{7}$$

With $Q^-_{i+1/2}$ and $Q^+_{i+1/2}$ defined, Roe's[17] approximate Riemann solver can easily be used to construct the desired numerical flux function $\tilde{F}_{i+1/2}$:

$$\begin{aligned}\tilde{F}_{i+\frac{1}{2}} &= F_n\left(Q^-_{i+\frac{1}{2}}, N_{i+\frac{1}{2}}\right) + \sum_m \lambda^{m-}_{i+\frac{1}{2}}\sigma^m_{i+\frac{1}{2}} r^m_{i+\frac{1}{2}} \\ &= F_n\left(Q^+_{i+\frac{1}{2}}, N_{i+\frac{1}{2}}\right) - \sum_m \lambda^{m+}_{i+\frac{1}{2}}\sigma^m_{i+\frac{1}{2}} r^m_{i+\frac{1}{2}} \\ &= \frac{1}{2}\left[F_n\left(Q^-_{i+\frac{1}{2}}, N_{i+\frac{1}{2}}\right) + F_n\left(Q^+_{i+\frac{1}{2}}, N_{i+\frac{1}{2}}\right)\right] \\ &\quad - \frac{1}{2}\left[\sum_m \left(\lambda^{m+}_{i+\frac{1}{2}} - \lambda^{m-}_{i+\frac{1}{2}}\right)\sigma^m_{i+\frac{1}{2}} r^m_{i+\frac{1}{2}}\right]\end{aligned} \tag{8}$$

An implicit scheme using Newton subiteration is adopted as the time-marching algorithm. From time step n to $n+1$, a number of Newton subiterations are required to achieve time accuracy. The semidiscretized system of Eq. (5), during each subiteration when marching from time n to time $n+1$, can be linearized about a known state Q^n to yield

$$\left[\frac{V^{n+1}}{\Delta t} + \frac{\partial R(Q^s)}{\partial Q}\right]\Delta Q^s = -\left[\frac{Q^s V^s - Q^n V^n}{\Delta t} + I_\alpha R(Q^s) + (I - I_\alpha)R(Q^n)\right] = \mathrm{res}(Q^s) \tag{9}$$

where the superscript n denotes the nth time level. As the residual $\mathrm{res}(Q^s)$ defined in Eq. (9) is driven below a predetermined error bound, the solution Q^{s+1} will be taken as the converged time-accurate solution Q^{n+1}. The constant α reflects the order of accuracy in time. The present scheme uses the second-order trapezoidal method, which requires that $\alpha = 0.5$. An approximate lower–upper factorization scheme[18] is employed to factorize the left-hand side of Eq. (9). The accuracy of the present code had been validated.[19]

III. Boundary Condition and Sound Source Modeling

In the present work, sound waves emitted from a body surface can be conceived as resulting from a fluctuating volume flux (blowing and suction) whose strength is specified. In other words, the sound source pertaining to the present problem is of the monopole type, as classified in the context of acoustics. The wall boundary condition treatment designed by Lu and Yeh[15] is employed. For the present cell-centered finite volume discretization, Euler simulation requires the pressure flux be evaluated over the monopole region. Basically, acoustic accuracy demands a delicate treatment in evaluating the pressure gradient around the monopole surface region. Any inaccuracy incurred in this sound source modeling will turn into spurious numerical waves emitted into the flowfield. The present numerical sound modeling is found very accurate, as demonstrated in many previous investigations.[9,10,13,15]

For the present simulation of acoustically excited unsteady flow, at the inlet and outlet boundaries the nonreflective boundary condition treatment of Fan and Lakshminarayana[20] is employed. This three-dimensional unsteady nonreflective boundary condition is an extension of the two-dimensional version originally proposed by Giles.[21] When this nonreflective boundary condition is implemented, note that upwind treatment ought to be employed not only in the inflow/outflow streamwise direction, but also in the lateral directions so as to ensure the numerical stability.[13]

IV. Dynamic Grid Method

In the simulation of vibrational problems, the grid system is altered due to either rigid-body motion or elastic deformation. According to Eq. (2), the flux across the interface is seen to be affected by the grid speed. A careful estimation of boundary grid speed is needed to avoid numerical errors induced by the moving meshes. In addition to the fundamental physical conservation laws that have to be satisfied, a requirement of geometric conservation[22,23] should also be incorporated. The geometric conservation law states that

$$V(t_2) - V(t_1) = \int_{t_1}^{t_2}\oint \boldsymbol{n}\cdot\boldsymbol{v}_g \,\mathrm{d}S\,\mathrm{d}t \tag{10}$$

where $[V(t_2) - V(t_1)]$ is the cell volume alteration during the time interval $\Delta t = t_2 - t_1$ and $\mathrm{d}S$ is the differential area of the cell boundary surface. Another constraint condition accompanying Eq. (10) is that the deforming cells should be closed in any instance,

$$\oint \boldsymbol{n}\,\mathrm{d}S = 0 \tag{11}$$

where $\boldsymbol{n}$ is the unit normal on the cell interface. In the construction of a dynamic mesh flow solver, the boundary velocities should be defined so that Eqs. (10) and (11) are strictly satisfied at the finite volume level.

In the present study, the grid nodal coordinates and the cell volumes $V(t_2)$ and $V(t_1)$ are known before time marching; hence, the individual averaged grid speed $\boldsymbol{v}_g \cdot \boldsymbol{n}$ at each cell face can be calculated using the following formula:

$$\Delta V_k = \int_{t_1}^{t_2} = \boldsymbol{n} \cdot \boldsymbol{v}_g S_k\,\mathrm{d}t, \qquad k = 1, 2, \ldots, 6 \tag{12}$$

where S_k is the area of the kth bounding surface. The time-averaged normal velocity of the cell boundary can, thus, be obtained using Eq. (12):

$$(\boldsymbol{v}_g \cdot \boldsymbol{n})_{S_k} \equiv \tilde{v}_n = \Delta V_k / \tilde{S}_k \Delta t \tag{13}$$

Note that there exists certain arbitrariness in defining the cell boundary area $\tilde{S}_k$. For an explicit scheme, $\tilde{S}_k = S_k^{(n)}$, and otherwise $\tilde{S}_k = S_k^{(n+1)}$ for an implicit scheme. The present scheme uses the implicit form.

V. Results and Discussion

A. NASA Rotor 67 Configuration and the Mean Flow

The focus of the present work is to examine the ducted rotor flowfield under acoustic excitations. Numerical simulation will be conducted to investigate the acoustically excited flowfield of a NASA rotor 67 transonic fan. This rotor is the first-stage rotor of a two-stage fan, designed and thoroughly tested at NASA Lewis Research Center.[24] Rotor 67 has 22 blades and was designed to operate at peak efficiency with a pressure ratio of 1.63 and a mass flow of 33.25 kg/s, rotating at a speed of 16,043 rpm. Many numerical simulations have been performed using rotor 67 experimental data as a benchmark standard.[25–27]

Rotor 67 was simulated in the present work with no inlet guide vanes and downstream stators. An H-type grid ($97 \times 36 \times 42$) was generated for a single blade passage, and the surface grids are shown in Fig. 1. Velocity and length scales used for the present nondimensionalization are the freestream sound speed a_∞ and the shroud radius R_1 upstream (station 1 defined in Ref. 24). In the following Euler calculations, it is assumed that there is no tip clearance and that the shroud rotates synchronously with the blades. The steady solution at the peak efficiency was computed. Figure 2 shows the comparison of the computed and experimental distributions of static pressure, total pressure, total temperature, and flow angle at the rotor exit plane. In general, an excellent overall agreement is achieved.

B. Acoustic Forcing

In this section, the behavior of rotor 67 under acoustic excitation is studied. The peak-efficiency steady-state flow was used as the mean stream to be acoustically perturbed. The acoustic forcing methods include both internal (sound source flush mounted in the blade surface) and external (sound source installed on engine casing or rotor hub) excitations. The monopole strength of this harmonic excitation is represented by $Q(t) = Q_0 \sin(kt)$, in which Q_0 is the nondimensionalized forcing amplitude. Note that, for the present acoustic application, $Q_0 = 5.78 \times 10^{-4}$ is equivalent to about 1% of the volume flow rate inhaled from the inlet of each blade passage. As for external shroud excitations, there are five locations that are selected for placing the monopole sources. These five excitation locations, shown in Fig. 3a, are $X_c = 0.14$ (near leading edge), 0.47 (near midchord), 0.9 (near trailing edge), and 1.21 and 1.74 (downstream areas). There is only one internal excitation location ($X_c = 0.9$) selected for simulation because we previously concluded[13] that trailing-edge forcing is the most effective internal forcing strategy.

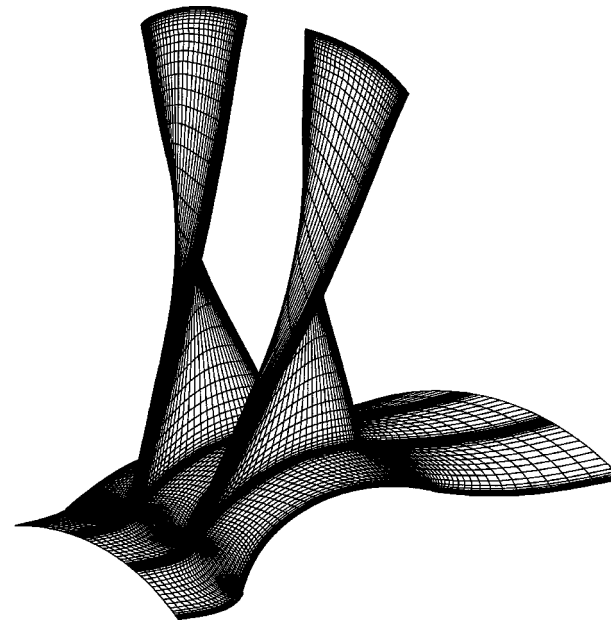

Fig. 1 Computational grid ($97 \times 36 \times 42$) of NASA rotor 67.

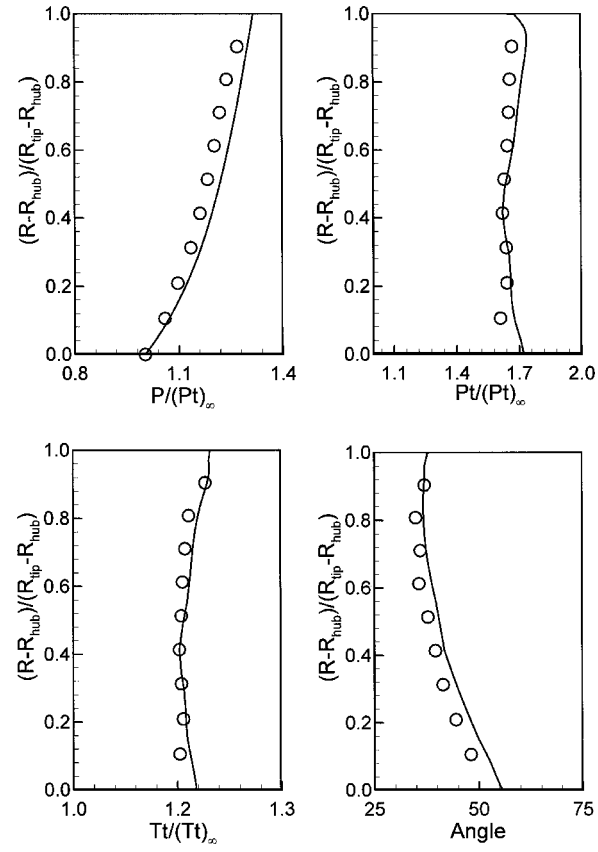

Fig. 2 Static pressure, total pressure, total temperature, and flow angle distribution, NASA rotor 67, near peak efficiency: circle, experiment and line, computation.

To examine the effectiveness of acoustic forcing, the unsteady torque C_θ and torsion C_m coefficients were computed and presented. Here, the torque is defined as the moment about the blade rotational axis, and the torsion is defined as the moment about an arbitrarily chosen axis, which is a radial line originating perpendicularly from

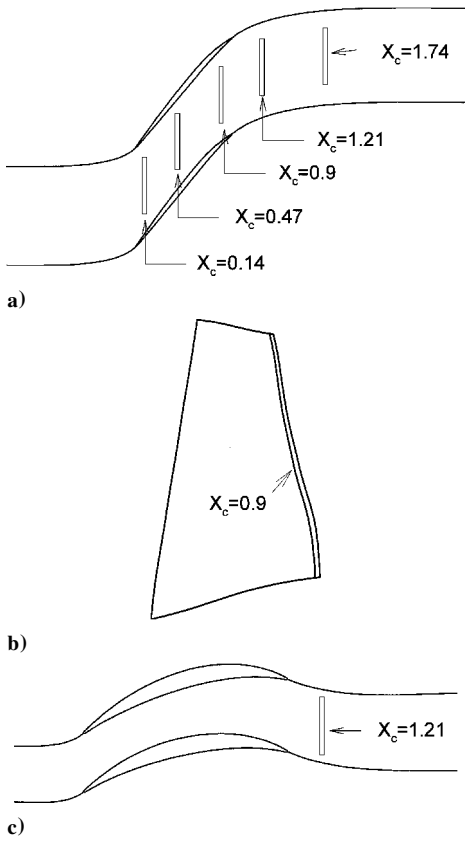

Fig. 3 Forcing locations of a) shroud excitation, b) blade excitation, and c) hub excitation.

the rotational axis and passing through the midpoint of the root chord on the hub. The parametric studies to be carried out include the arrangement of the sound source locations and the effects of reduced frequency, source strength, and forcing location, as discussed in the following sections.

1. Effect of Sound Source Arrangement

The acoustically induced airloads resulting from forcings with different slot (continuous) or perforated (discrete) sound source arrangements are shown in Figs. 4 and 5. In these simulated cases, equal overall sound source strengths are assumed while making comparisons. In Figs. 4 and 5, $P2$ and $P3$ are defined as one acoustic source per two cells and per three cells, respectively, along the circumferential direction for the external shroud excitation. Similarly, the acoustic sources were arranged around the blade trailing edge for internal (suction side) excitation. Figures 4 and 5 indicate that the unsteady C_θ and C_m coefficients are almost identical except at the peak values. Generally speaking, the more uniform are the sources distributed, the better will be the excitation effect achieved. Nevertheless, in the practical implementation, the structural integrity should be considered. A long slot would cause more structural problems than does an array of discrete holes. Hence, there exists some structural design compromise that a finite number of discrete sound sources might be adopted as internal excitation to be used.

2. Shroud Forcing Mechanism

To understand the shroud forcing mechanism, a numerical simulation of a duct flow under acoustic excitation was examined. The sound source was mounted on the duct wall. The excitation route along which the acoustic disturbances travel internally in a ducted transonic mean flow is shown in Fig. 6. In this transonic case the tip and hub stream Mach numbers are 1.4 and 0.6, respectively. It is clearly seen in the snapshot pictures that the disturbances propagate downstream initially along the Mach lines, and then induce upstream influence while interacting with the subsonic part of the

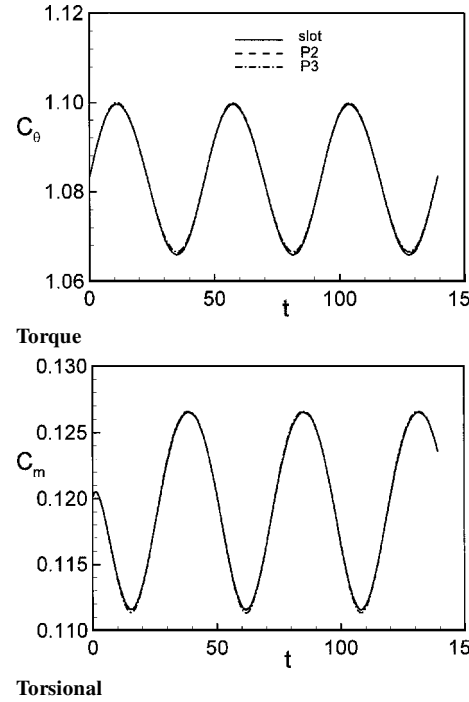

Fig. 4 Unsteady moment coefficients induced by acoustic excitation on NASA rotor 67, shroud forcing; $Q(t) = Q_0 \sin(kt)$, $Q_0 = 5.78 \times 10^{-4}$, and $k = 0.1355$ and $X_c = 1.21$.

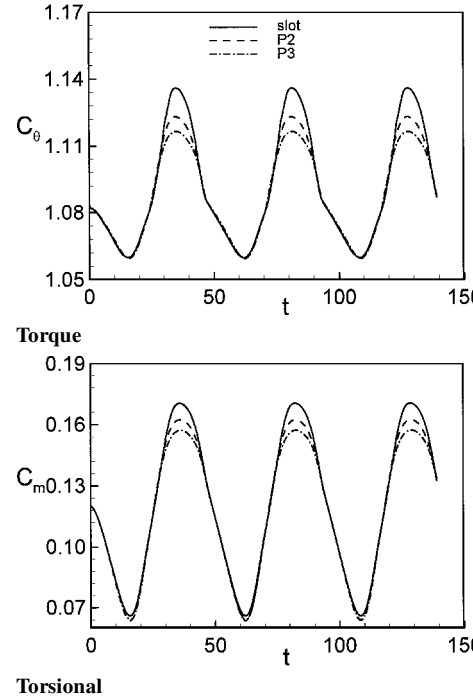

Fig. 5 Unsteady moment coefficients induced by acoustic excitation on NASA rotor 67, suction side forcing; $Q(t) = Q_0 \sin(kt)$, $Q_0 = 5.78 \times 10^{-4}$, and $k = 0.1355$ and $X_c = 1.21$.

flowfield. The subsonic core flow actually serves as an embedded corridor, which backtransmits the acoustic pressure fluctuation sent by the monopole mounted over the supersonic duct wall region. The subsonic corridor, as perturbed by the induced downstream excitation, will interact with its outer confining supersonic stream and form a closed-loop-typemutual interaction. The resultant flowfield, as demonstrated in Fig. 6e, shows a very vertically aligned pattern of Mach lines near the forcing location.

Note that in a subsonic duct flow the acoustic disturbance would not die out so long as it is excited by a cut-on frequency sound source. This nondecaying duct acoustic behavior can explain why

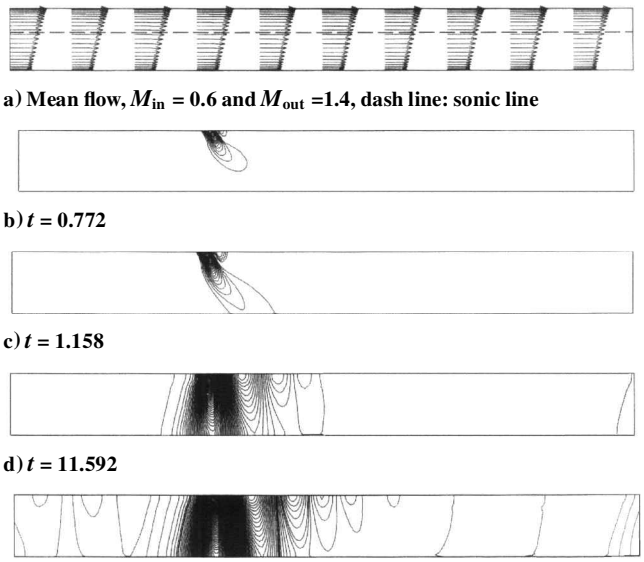

a) Mean flow, M_{in} = 0.6 and M_{out} =1.4, dash line: sonic line

b) t = 0.772

c) t = 1.158

d) t = 11.592

e) t = 15.456

Fig. 6 Pressure fluctuation distribution for monopole radiation in a duct with transonic mean flow; $Q(t) = Q_0 \sin(kt)$, $Q_0 = 8.8 \times 10^{-3}$, and $k = 0.1355$.

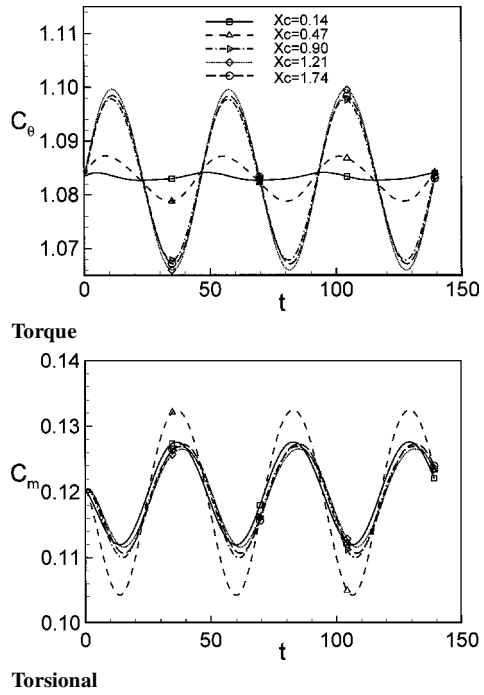

Fig. 7 Unsteady moment coefficients induced by acoustic excitation on NASA rotor 67, shroud forcing; $Q(t) = Q_0 \sin(kt)$, $Q_0 = 5.78 \times 10^{-4}$, and $k = 0.1355$.

the excitation effects remain almost unchanged as the shroud forcing location is placed downstream beyond the trailing edge of the blade, as shown in Fig. 7.

3. Optimal Shroud Forcing Location

Shown in Fig. 7 are the time-dependent C_θ and C_m histories induced by sound waves emitted from various monopoles located on the engine casing. It has been well understood that, in turbomachinery flow, the potential interaction is relatively stronger as acoustic waves are propagated from the downstream. By the same argument and also supported by the results of Fig. 7, the downstream location is shown to be a better forcing place for the present external acoustic excitations. Unlike the internal forcing cases, an effective external excitation can easily be achieved so long as the sound source is situated in the downstream beyond the trailing edge of the forced blades.

4. Acoustic Energy Supply

Figure 8 shows the acoustic strength effect associated with shroud excitations. The induced airloads are seen enlarged, however, not in a strict linear manner, as the forcing strength increases. This slight nonlinearity is attributed to the shock excursion effect occurring at the midspan region where weak transonic shock can be moved by acoustic excitations. (This shock excursion phenomenon was observed using a movie made from the simulated data.)

How much acoustic energy ought to be supplied for flutter suppression is a concern in the practical design of the acoustic actuator system. It was concluded in a previous investigation[9] that an effective suppression can only be achieved when the flutter amplitude is small. This constraint simply comes from the nature of the acoustics, namely, the pressure fluctuation of a sound wave is in general very small. Here, we use the energy content to measure the power consumption of an acoustic device:

$$\int_V \left(\frac{\partial E}{\partial t} + \nabla \cdot \boldsymbol{I} \right) \mathrm{d}V = \sum_i p_i' Q_i \tag{14}$$

where E and I are the acoustic energy and acoustic flux vectors, respectively.[28] This relationship describes the energy contents of the stored acoustic energy in the control volume,

$$\int_V E \, \mathrm{d}V$$

the energy flux across the control surface,

$$\oint_s \boldsymbol{I} \cdot \boldsymbol{n} \, \mathrm{d}S$$

and the acoustic energy supplied by a monopole,

$$\sum_i p_i' Q_i$$

where p_i' and Q_i are the fluctuation pressure and the volume flow rate of the ith constituent cell of the monopole.

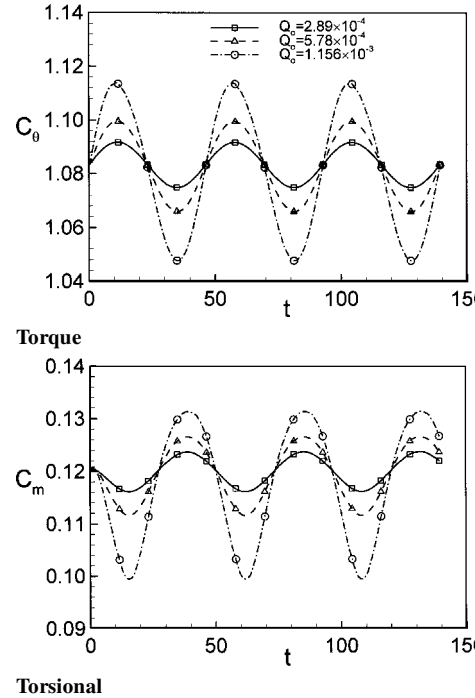

Fig. 8 Unsteady moment coefficients induced by acoustic excitation on NASA rotor 67, shroud forcing; $Q(t) = Q_0 \sin(kt)$, $k = 0.1355$, and $X_c = 1.21$.

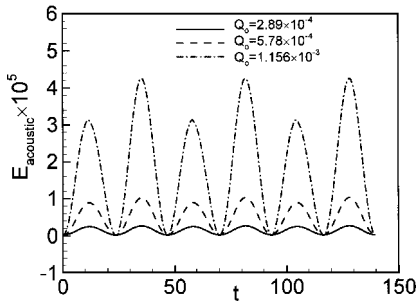

Fig. 9 Acoustic energy supply histories of an acoustic excitation on NASA rotor 67, shroud forcing; $Q(t) = Q_0 \sin(kt)$, $k = 0.1355$, and $X_c = 1.21$.

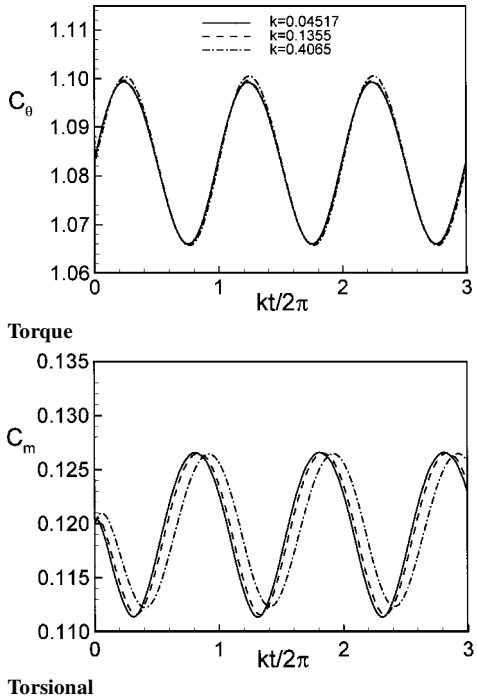

Fig. 10 Unsteady moment coefficients induced by acoustic excitation on NASA rotor 67, shroud forcing; $Q(t) = Q_0 \sin(kt)$, $Q_0 = 5.78 \times 10^{-4}$, and $X_c = 1.21$.

The power supply required for actuating monopole sources located on the engine casing is shown in Fig. 9. For the baseline strength $Q_0 = 5.78 \times 10^{-4}$, which corresponds to 1% of the inlet volume flow rate, the maximum amplitude of the power required, as nondimensionalized by $\rho_\infty a_\infty^3 R_1^2$, is around 1×10^{-5}, equivalent to 32.3-W power output per blade as the engine is operated at the standard sea-level ambient condition.

5. Effect of Reduced Frequency

It has been generally concluded in unsteady aerodynamic research that the induced unsteady airloads are diminishing as the forcing frequency increases.[29] Aerodynamically, this is caused by the inability of the flow inertia to respond fully when a high-frequency forcing mechanism is introduced. Figures 10 and 11 show the resultant airloads as the rotor is externally or internally excited. It is observed that, for the present turbomachinery flowfield, the differences in C_θ and C_m under various forcing frequencies are less apparent than those obtained in the externally unbounded flows.[10] When the casing and blade forcing results are compared, it can be found that the unsteady flow phenomena are more eminent when excited internally, hence showing a relatively marked difference between the induced C_θ and C_m distributions because the excitation location is placed much closer to the most sensitive trailing-edge region.

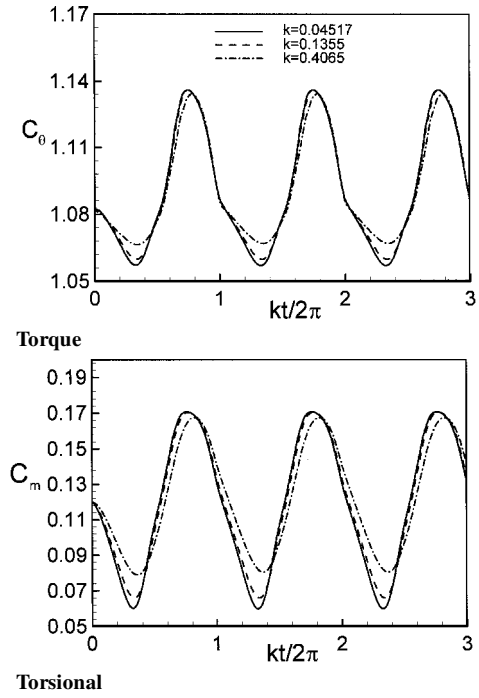

Fig. 11 Unsteady moment coefficients induced by acoustic excitation on NASA rotor 67, suction side forcing; $Q(t) = Q_0 \sin(kt)$, $Q_0 = 5.78 \times 10^{-4}$, and $X_c = 0.9$.

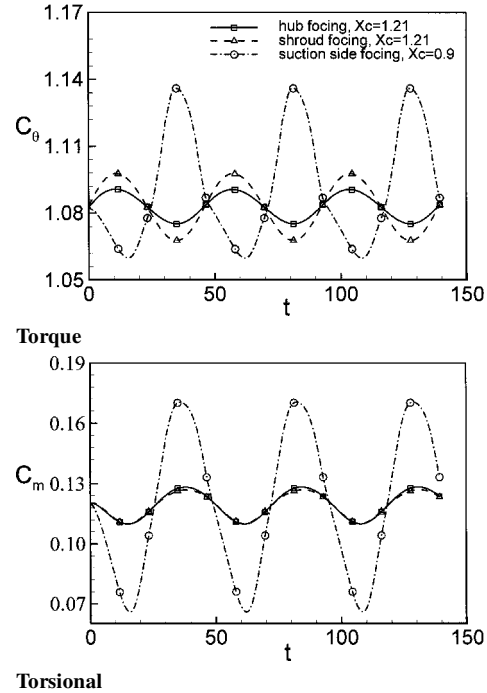

Fig. 12 Unsteady moment coefficients induced by acoustic excitation on NASA rotor 67; $Q(t) = Q_0 \sin(kt)$, $Q_0 = 5.78 \times 10^{-4}$, and $k = 0.1355$.

6. Effectiveness Comparison Between Internal and External Excitations

Figure 12 shows the unsteady airloads resulting from forcings at different excitation locations on hub, shroud, and blade areas. Trailing-edge forcing is seen more effective when compared to hub or shroud excitation. It is shown that the amplitude of C_m induced by blade excitation is at least four times larger than those generated by hub and shroud excitations. Shown in Fig. 13 is the amplitude of the first harmonic associated with the aerodynamic derivative of shroud and blade excitations, respectively. These derivatives provide a quantitative evaluation of how effective the excitation is. External

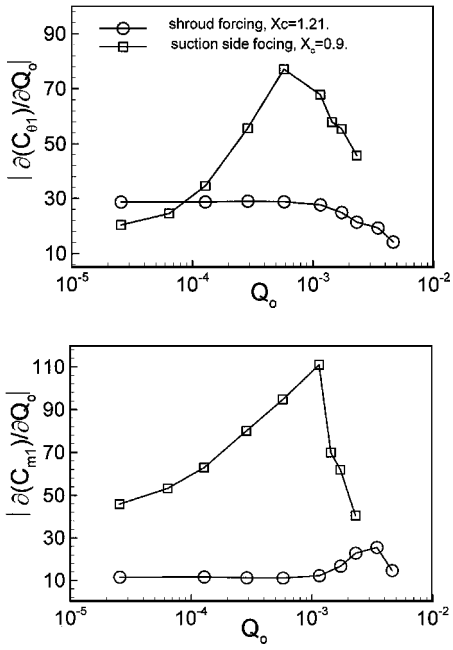

Fig. 13 Aerodynamic derivative vs forcing amplitude Q_0 for NASA rotor 67; $Q_t = Q_0 \sin(kt)$ and $k = 0.1355$: a) torque (first harmonic) $|\partial(C_{\theta 1})/\partial Q_0|$ and b) torsional moment (first harmonic) $|\partial(C_{m1})/\partial Q_0|$.

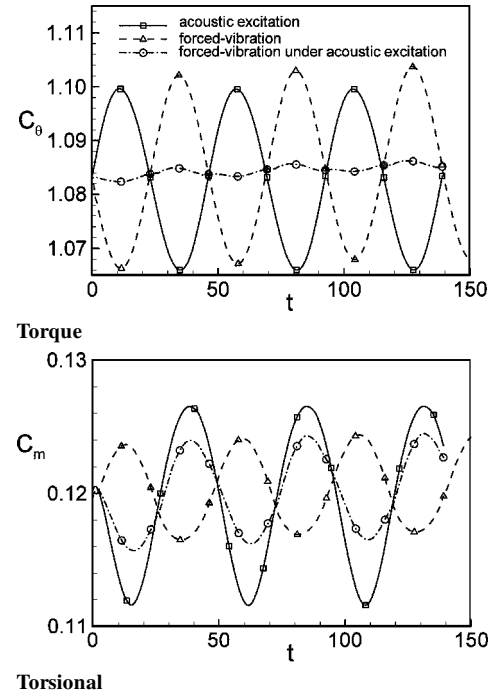

Fig. 14 Unsteady moment coefficients induced by acoustic excitation and forced vibration for NASA rotor 67, shroud forcing; acoustic excitation, $Q(t) = Q_0 \sin(kt)$, $Q_0 = 5.78 \times 10^{-4}$, and $k = 0.1355$ and $X_c = 1.21$; forced vibration, $\alpha(t)_{\text{tip}} = \alpha_0 \sin(kt)$, and $\alpha_0 = 0.008$ rad and $k = 0.1355$.

excitation possesses a wider range of linearity than does the internal alternative. This is because that the acoustic disturbances, as emitted and propagated externally from a distant sound source, remain small when encountering the solid blade. At the present time, it is premature to conclude which excitation method is better. Perhaps, the choice might depend on the manufacturing technique available. Suppose a miniaturized sound generator can be made and installed without any material or delamination problems around the trailing edge, internal excitation will be an ideal candidate. Otherwise, forcing via mounting loudspeakers on the engine casing would be more realistic.

C. External Acoustic Flutter Suppression

To demonstrate that flutter suppression can be achieved by means of acoustic excitation, the energy content of a forced pitching oscillation of the NASA rotor 67 is examined. The blade is forced to oscillate about a hypothetical torsional axis defined previously. The amplitude of oscillation is assumed linearly varing from 0 rad at the hub to 0.008 rad at the tip. The reduced frequency is set equal to 0.1355, and the forced vibration is described by the harmonic angular oscillation,

$$\alpha(r, t) = \alpha_0(r) \sin(kt) \tag{15}$$

The work per cycle is defined as

$$W_{\text{percycle}} = -\int_0^T \oint p\boldsymbol{n} \cdot \boldsymbol{u} \, \mathrm{d}S \, \mathrm{d}t \tag{16}$$

in which, p is the unsteady pressure and $\boldsymbol{u}$ the oscillating surface velocity relative to the pitching axis. A positive value of W_{percycle} means energy is stored in the blade or the system is unstable and vice versa for a stabilized system.

A forced torsional motion under acoustic excitation is investigated. Here, the mean stream is still the peak-efficiency steady-state flow. The shroud acoustic excitation conditions adopted are $Q_0 = 5.78 \times 10^{-4}$, $k = 0.1355$, $Q = Q_0 \sin(kt)$, and $X_c = 1.21$. Shown in Fig. 14 are the unsteady loadings induced either by a pure forced vibration, a pure acoustic excitation (blade fixed), or an acoustically controlled forced vibration. The unsteady airloads due to acoustic excitation is seen out-of-phase relative to that due

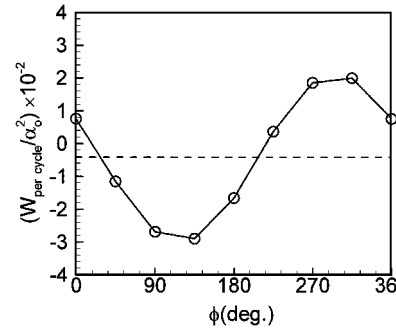

Fig. 15 Work per cycle for the NASA rotor 67, forced-vibration under acoustic excitation shroud forcing, $Q(t) = Q_0 \sin(kt + \phi)$, $Q_0 = 5.78 \times 10^{-4}$, $k = 0.1355$, $X_c = 1.21$, $\alpha(t)_{\text{tip}} = \alpha_0 \sin(kt)$, and $\alpha_0 = 0.008$ rad.

to forced vibration. The C_θ and C_m amplitudes of the acoustically controlled torsional vibration are approximately equal to the sum contributed by the pure acoustic excitation and the forced vibration. This indicates that nolinearity is weak and that the superpositional principle still prevails under such strength of forcing.

The work per cycle of the original forced vibration is negative, as shown in Fig. 15 (dashed line). This negative work means that the rotor blade at this oscillation frequency is stable. Because active control is considered in the present acoustic flutter suppression, the monopole strength should vary in response to the sensed state. For the present single-degree-of-freedom torsional oscillation, the control law selected is

$$Q(t) = G_\alpha \alpha(kt + \phi) \tag{17}$$

in which G_α is the gain amplitude and ϕ the gain phase of the control logic. In the simulated acoustic control cases, we choose $G_\alpha = 0.7225$, which corresponds to a strength of $Q_0 = 5.78 \times 10^{-4}$ for a vibrational amplitude of $(\alpha_0)_{\max} = 0.008$ rad. The work per cycle for the acoustically controlled forced vibration is shown in Fig. 15. The gain phase ϕ plays a critical role in dictating the stability of the closed-loop dynamic system. For the present case investigated, the stabilizing phase resides between $30 < \phi < 210$ deg.

The most effective stabilizing phase is found around $\phi = 135$ deg. Under this optimal excitation condition, the maximum amplitude of the power required is equal to 37.2 W per blade. As indicated in Fig. 15, the flutter margin can be enlarged nearly six times when acoustically forced using this optimal gain phase ($\phi \approx 135$ deg).

VI. Conclusions

A ducted NASA rotor 67 fan was used as the model to examine the feasibility of suppressing transonic flutter instability by means of acoustic excitations. Both internal and external forcing simulations were performed and analyzed. Internal forcing is found more effective than external, disregarding the disadvantages and difficulties contained in hardware implementation. External forcing is modeled by placing sound sources on either engine casing or rotor hub. The physical mechanism associated with external shroud forcing is explained, and it is found that downstream forcing is more effective. A forced vibration together with shroud excitation is conducted to assess the acoustic flutter suppression capability. It is found that, as appropriate control phase is employed, the fluttering motion can be acoustically suppressed. The present numerical investigation achieves an initial understanding of the physical mechanism associated with the turbomachinery acoustic flutter control technique. Important issues such as optimal excitation location, forcing frequency effect, control gain amplitude and phase, and acoustic energy supply requirements have been discussed. These basic findings will be helpful for the future hardware realization of the present acoustic method.

Acknowledgments

This work is supported by the National Science Council under Contract NSC 89-2212- E006-186. The authors are very appreciative of many valuable suggestions provided by Ron-Ho Ni of Pratt and Whitney Aircraft, United Technologies, during the course of this research.

References

[1]Huang, X.-Y., "Active Control of Aerofoil Flutter," *AIAA Journal*, Vol. 25, No. 8, 1987, pp. 1126–1132.

[2]Bendiksen, O. O., "Flutter of Mistuned Turbomachinery Rotors," *Journal of Engineering for Gas Turbines and Power*, Vol. 106, No. 1, 1984, pp. 25–33.

[3]Sinha, A., and Griffin, J. H., "Effects of Friction Dampers on Aerodynamiclly Unstable Rotor Stages," *AIAA Journal*, Vol. 23, No. 2, 1985, pp. 262–270.

[4]Bendiksen, O. O., and White, J. F., III, "Aeroelastic Tailoring of Advanced Composite Compressor Blades," *Proceeding of the 27th AIAA/ASME/ASCE/AHS Structures, Structural Dynamics, and Materials Conference*, AIAA, Washington, DC, 1986, pp. 684–692.

[5]Nagai, K., Toshimitsu, K., and Namba, M., "Active Control of Cascade Flutter by Means of Sound Waves from Duct Wall Sources," *Japan Society of Mechanical Engineers International Journal*, Ser. B, Vol. 39, No. 3, 1996, pp. 608–614.

[6]Toshimtsu, K., Otsuka, T., Maruo, H., and Namba, M., "Active Control of Low Frequency Blade Flutter by Acoustic Excitation," *Technology Reports of Kyushu University*, Vol. 72, No. 2, 1999, pp. 109–114.

[7]Ffowcs Williams, J. E., "Acoustic Control of Flow Instabilities," *Unsteady Aerodynamics, Aeroacoustics, and Aeroelasticity of Turbomachines and Propellers*, edited by H. M. Atassi, Springer-Verlag, New York, 1993, pp. 643–653.

[8]Lu, P.-J., and Huang, L.-J., "Flutter Suppression of Thin Airfoils Using Active Acoustic Excitations," *AIAA Journal*, Vol. 30, No. 12, 1992, pp. 2873–2881.

[9]Lu, P.-J., Pan, D., and Yeh, D.-Y., "Transonic Flutter Suppression Using Active Acoustic Excitations," *AIAA Journal*, Vol. 33, No. 4, 1995, pp. 694–702.

[10]Yeh, D.-Y., "Unsteady Aerodynamic and Aeroelastic Behaviors of Acoustically Excited Transonic Flow," Ph.D. Dissertation, Dept. of Aeronautics and Astronautics, National Cheng Kung Univ., Taiwan, ROC, 1992.

[11]Nagai, K., Toshimitsu, K., and Namba, M., "Active Suppression of Cascade Flutter by Means of Sound Waves from Duct Wall Sources," *Unsteady Aerodynamics and Aeroleasticity of Turbomachines*, edited by Y. Tanida and N. Namba, Elsevier, Amsterdam, 1995, pp. 565–581.

[12]Lu, P.-J., and Chen, S.-K., "Evaluation of Acoustic Flutter Suppression in Transonic Cascade Flows," *Proceedings of the 6th International Symposium on Transport Phenomena and Dynamics of Rotating Machinery*, Honolulu, Vol. 2, 1996, pp. 355–364.

[13]Chen, S.-K., "Acoustic Flutter Suppression of Cascade in Inviscid and Viscous Transonic Flows," Ph.D. Dissertation, Dept. of Aeronautics and Astronautics, National Cheng Kung Univ., Taiwan, ROC, 1999.

[14]Gad-el-Hak, M., and Bushnell, D. M., "Separation Control: Review," *Journal of Fluid Engineering*, Vol. 113, No. 1, 1991, pp. 5–31.

[15]Lu, P.-J., and Yeh, D.-Y., "Numerical Simulation of Trailing-Edge Acoustic/Vortical Interaction," *AIAA Journal*, Vol. 33, No. 5, 1995, pp. 785–793.

[16]Chakravarthy, S. R., and Osher, S., "New Class of High Accuracy TVD Schemes for Hyperbolic Conservation Laws," AIAA Paper 85-0363, 1985.

[17]Roe, P. L., "Approximate Riemann Solvers, Parameter Vectors, and Difference Schemes," *Journal of Computational Physics*, Vol. 43, No. 2, 1981, pp. 357–372.

[18]Pan, D., and Lomax, H., "A New Approximate LU Factorization Scheme for the Reynold- Averaged Navier–Stokes Equations," *AIAA Journal*, Vol. 26, No. 2, 1988, pp. 163–171.

[19]Pan, D., Lu, P.-J., You, H.-D., and Tung, S.-F., "Parallel Computation of Euler Flow on a PC Cluster," *Proceedings of the Sixth National Computational Fluid Dynamics Conference*, 1999, Taitung, Taiwan, pp. 145–149.

[20]Fan, S., and Lakshminarayana, B., "Time-Accurate Euler Simulation of Interaction of Nozzle Wake and Secondary Flow with Rotor Blade in an Axial Turbine Stage Using Nonreflecting Boundary Condition," *Journal of Turbomachinery*, Vol. 118, No. 4, 1996, pp. 663–678.

[21]Giles, M. B., "Nonreflecting Boundary Conditions for Euler Equation Calculations," *AIAA Journal*, Vol. 28, No. 12, 1990, pp. 2050–2058.

[22]Thomos, P. D., and Lombard, C. K., "Geometric Conservation Law and its Application to Flow Computations on Moving Grids," *AIAA Journal*, Vol. 17, No. 10, 1979, pp. 1030–1037.

[23]Vinokur, J. M., "Review Article: An Analysis of Finite-Difference and Finite-Volume Formulation of Conservation Law," *Journal of Computational Physics*, Vol. 81, No. 1, 1989, pp. 1–52.

[24]Strazisar, A. J., Wood, J. R., Hathaway, M. D., and Suder, K. L., "Laser Anemometer Measurements in a Transonic Axial-Flow Rotor," NASA TP 2879, 1989.

[25]Weber, K. F., Thoe, D. W., and Delaney, R. A., "Analysis of Three-Dimensional Turbomachinery Flows on C-Type Grids Using an Implicit Euler Solver," *Journal of Turbomachinery*, Vol. 112, No. 3, 1990, pp. 362–369.

[26]Chima, R. V., "Viscous There-dimensional Calculations of Transonic Fan Performance," AGARD, Paper 21, 1991.

[27]Hah, C., and Reid, L., "Viscous Flow Study of Shock–Boundary Layer Interaction, Radial Transport, and Wake Development in a Transonic Compressor," *Journal of Turbomachinery*, Vol. 114, No. 3, 1992, pp. 538–547.

[28]Goldstein, M. E., Aeroacoustics, McGraw–Hill, New York, 1976, Chap. 2, pp. 39–42.

[29]Tijdeman, H., and Seebass, R., "Transonic Flow Past Oscillating Airfoils," *Annual Review of Fluid Mechanics*, Vol. 12, 1980, pp. 181–222.